Dirac monopoles with a polar-core vortex induced by spin-orbit coupling in spinor Bose-Einstein condensates

Ji Li,[1,2] Yan-Mei Yu,[1,2] Lin Zhuang,[3] and Wu-Ming Liu[1,2,*]

[1]*Beijing National Laboratory for Condensed Matter Physics, Institute of Physics, Chinese Academy of Sciences, Beijing 100190, China*
[2]*School of Physical Sciences, University of Chinese Academy of Sciences, Beijing 100190, China*
[3]*School of Physics, Sun Yat-Sen University, Guangzhou 510275, People's Republic of China*

We report Dirac monopoles with a polar-core vortex induced by spin-orbit coupling in ferromagnetic Bose-Einstein condensates, which are attached to two nodal vortex lines along the vertical axis. These monopoles are more stable in the time scale of experiment and can be detected through directly imaging vortex lines. When the strength of spin-orbit coupling increases, Dirac monopoles with a vortex can be transformed into those with a square lattice. In the presence of spin-orbit coupling, increasing the strength of the interaction can induce a cyclic phase transition from Dirac monopoles with a polar-core vortex to those with a Mermin-Ho vortex. The spin-orbit coupled Bose-Einstein condensates not only provide a unique platform for investigating exotic monopoles and relevant phase transitions but also can hold stable monopoles even though a quadrupole field is turned off.

I. INTRODUCTION

Dirac monopoles have drawn great interest in solid state physics [1–8], quantum field [9,10], and gauge field theories [11–13]. In particular, the recent realization of spinor Bose-Einstein condensates (BECs) has brought a new way to create monopoles [14,15] and topologically nontrivial structures [16–19]. So far, monopoles with and without terminating nodal lines have been realized in BEC experiments [9,10]. Theoretically, several typical monopole structures like two-dimensional and two-component monopoles in BECs have been investigated [20–29]. In previous studies on monopoles only spin-dependent interaction has been considered, whereas spin-orbit (SO) coupling, i.e., the interaction between the spin of a quantum particle and its momentum, has not been considered in spinor BECs.

The SO coupling in quantum gases can be controlled by using optical or magnetic fields [30–40], which provides possibly new opportunities to search for novel quantum states [41–49]. These novel quantum states can be induced because of coupling of atomic internal states and momenta. Meanwhile, due to the SO coupling, atoms with pseudospins are not constrained by fundamental symmetries, like global and mirror symmetries. Therefore, novel monopole structures may be induced by the SO coupling in spinor BECs, which we are eager to explore.

In this paper, we find a configuration of monopoles, Dirac monopoles with a polar-core vortex, induced by the SO coupling in ferromagnetic BECs. Differently from the monopoles in the absence of the SO coupling [9,15], the monopoles in the SO coupled spinor BECs locate at the endpoints of two nodal lines along the vertical axis. The nodal lines remain stable for a very long time, indicating that the monopoles with the polar-core vortex are a long-lived structure. Therefore, experimental observation of the monopoles with a polar-core vortex will be easier, as compared with the monopole structures found in previous works in the absence of the SO coupling

[9,24]. Further, a monopole configuration with the square lattice is found for strong SO coupling. Such a configuration is independent of the strength of interactions and therefore can be observed in a wide range of parameters. In particular, a cyclic phase transition from the monopoles with the polar-core vortex to the monopoles with the Mermin-Ho vortex is found through increasing the strength of the spin-independent interaction when the SO coupling is weak.

II. DIRAC MONOPOLES WITH A POLAR-CORE VORTEX

We consider the three-dimensional spin-1 BECs with a two-dimensional SO coupling [38] and a controllable magnetic field [9]. In the mean-field approximation, the Hamiltonian is written as [15,23,24,41–43,50]

$$
H = \int d^3\mathbf{r} \bigg(\Psi^\dagger [T + V_{\text{opt}}(\mathbf{r}) + \mathcal{V}_{so} + g_F \mu_B \mathbf{B}(\mathbf{r}) \cdot \mathcal{F}] \Psi
$$
$$
+ \left\{ \frac{c_0}{2} n^2 + \frac{c_2}{2} [(n_1 - n_{-1})^2 + 2|\Psi_1^* \Psi_0 + \Psi_0^* \Psi_{-1}|^2] \right\} \bigg),
$$
(1)

where $\Psi = [\Psi_1(\mathbf{r}), \Psi_0(\mathbf{r}), \Psi_{-1}(\mathbf{r})]^T$ is the order parameter of the BECs with normalization $\int d^3\mathbf{r}\Psi^\dagger\Psi = N$, and N is the total particle number. The kinetic energy $T = -\hbar^2\nabla^2/(2m)$. The total particle density is defined by $n = \sum_m n_m$, wherein $n_m = |\Psi_m(\mathbf{r})|^2$ with $m = 0, \pm 1$. The optical trapping potential $V_{\text{opt}}(\mathbf{r}) = m[\omega_r^2(x^2 + y^2) + \omega_z^2 z^2]/2$, where ω_r and ω_z are the radial and axial trapping frequencies, and m is the mass of a ^{87}Rb atom. The vector of spin-1 matrices is defined by $\mathcal{F} = (\mathcal{F}_x, \mathcal{F}_y, \mathcal{F}_z)^T$, wherein $\mathcal{F}_x$, $\mathcal{F}_y$, and $\mathcal{F}_z$ are the 3 × 3 Pauli spin-1 matrices. The SO coupling term is written as $\mathcal{V}_{so} = -i\hbar(\kappa_x \mathcal{F}_x \partial_x + \kappa_y \mathcal{F}_y \partial_y)$, where κ_x and κ_y are the strengths of the SO coupling. We define $\kappa_x = \kappa_y = \kappa$ for isotropic SO coupling (Rashba-type) and $\kappa_x \neq \kappa_y$ for anisotropic SO coupling. The external magnetic field is given by $\mathbf{B}(\mathbf{r}) = B_1'(x\widehat{e_x} + y\widehat{e_y}) + B_2'z\widehat{e_z}$, where the condition $2B_1' + B_2' = 0$ must be satisfied according to Maxwell's equation $\nabla \cdot \mathbf{B} = 0$. The Land é factor $g_F = -1/2$ and μ_B is the Bohr magneton.
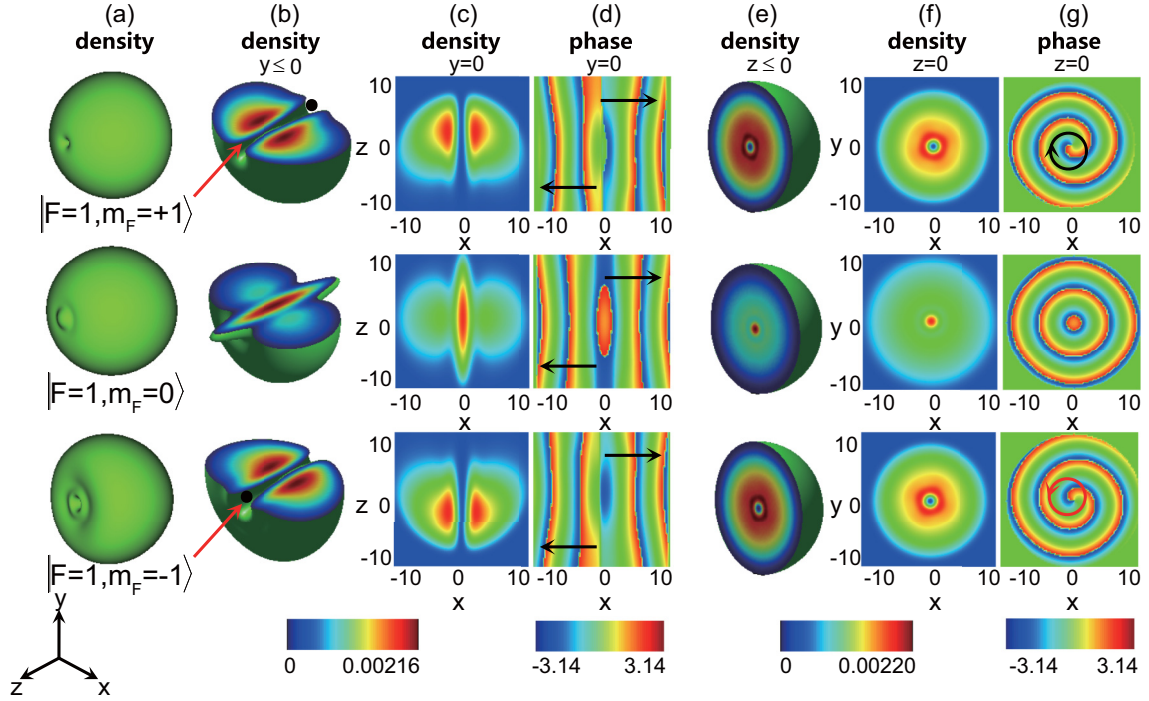
*wliu@iphy.ac.cn

FIG. 1. The monopoles with the polar-core vortex. (a) Isosurface of particle densities. (b) Particle densities for $y \leqslant 0$. The position of the nodal line (Dirac string) is highlighted by the red arrow. The position of the monopole is highlighted by the black dot. The result for $x \leqslant 0$ is the same as that for $y \leqslant 0$. (c) and (d) Densities and phase distributions in the $y = 0$ planes. The phases at both sides of the $y = 0$ planes are inverse, as highlighted by the black arrow in (d). (e) Particle densities for $z \leqslant 0$. (f) and (g) Densities and phase distributions in the $z = 0$ planes. The single vortex and antivortex are highlighted by the black and red circles, respectively. The simulation is conducted by using the dimensionless SO coupling strength $\kappa = 2$, spin-dependent interaction parameter $\lambda_2 = -75$, spin-independent interaction parameter $\lambda_0 = 7500$, strength of the magnetic field gradient $B_1 = 0.6$, and isotropic optical trap $\omega_r = \omega_z = 2\pi \times 250$ Hz [15].

For the interaction terms, the coupling parameters are given by $c_0 = 4\pi\hbar^2(a_0 + 2a_2)/3m$ and $c_2 = 4\pi\hbar^2(a_2 - a_0)/3m$, where $\hbar$ is the Planck constant and $a_{0,2}$ are two-body s-wave scattering lengths for total spin 0,2. The wave functions of spin-1 BECs are formulated as the dimensionless coupled Gross-Pitaevskii equations [15,23,24,41–43,50]

$$i\frac{\partial \psi_1}{\partial t} = \left[-\frac{1}{2}\nabla^2 + V + \lambda_0\rho + \lambda_2(\rho_1 + \rho_0 - \rho_{-1}) \right. $$
$$\left. + B_2 z \right]\psi_1 + B_1(x - iy)\psi_0$$
$$+ \kappa(-i\partial_x - \partial_y)\psi_0 + \lambda_2\psi_{-1}^*\psi_0^2, \qquad (2)$$

$$i\frac{\partial \psi_0}{\partial t} = \left[-\frac{1}{2}\nabla^2 + V + \lambda_0\rho + \lambda_2(\rho_1 + \rho_{-1}) \right]\psi_0$$
$$+ B_1(x + iy)\psi_1 + B_1(x - iy)\psi_{-1}$$
$$+ \kappa(-i\partial_x + \partial_y)\psi_1 + \kappa(-i\partial_x - \partial_y)\psi_{-1}$$
$$+ 2\lambda_2\psi_1\psi_{-1}\psi_0^*, \qquad (3)$$

$$i\frac{\partial \psi_{-1}}{\partial t} = \left[-\frac{1}{2}\nabla^2 + V + \lambda_0\rho + \lambda_2(\rho_0 + \rho_{-1} - \rho_1) \right. $$
$$\left. - B_2 z \right]\psi_{-1} + B_1(x + iy)\psi_0$$
$$+ \kappa(-i\partial_x + \partial_y)\psi_0 + \lambda_2\psi_1^*\psi_0^2, \qquad (4)$$

where the dimensionless wave function $\psi_j = N^{-1/2}a_h^{3/2}\Psi_j$ and the total condensate density $\rho = \rho_1 + \rho_0 + \rho_{-1}$ with $\rho_j = |\psi_j|^2 \, (j = 1, 0, -1)$. The dimensionless optical trapping potential $V(\mathbf{r}) = \frac{1}{2}(\gamma_r^2 x^2 + \gamma_r^2 y^2 + \gamma_z^2 z^2)$ with $\gamma_r = \omega_r/\omega$, $\gamma_z = \omega_z/\omega$ and $\omega = \min\{\omega_r, \omega_z\}$. The dimensionless interaction strengths $\lambda_0 = 4\pi N(a_0 + 2a_2)/3a_h$ and $\lambda_2 = 4\pi N(a_2 - a_0)/3a_h$. We choose $a_2 = (100.4 \pm 0.1)a_B$ for total spin channel $F_{\text{total}} = 2$ and $a_0 = (101.8 \pm 0.2)a_B$ for total spin channel $F_{\text{total}} = 0$ [51–53], where a_B is the Bohr radius. The characteristic length of the harmonic trap is defined as $a_h = \sqrt{\hbar/m\omega}$. The dimensionless strength of the magnetic field gradient complies the condition $2B_1 + B_2 = 0$. The time, energy, strength of the SO coupling, and strength of the magnetic field gradient are scaled by ω^{-1}, $\hbar\omega$, $\sqrt{\hbar\omega/m}$, and $\omega\hbar/(g_F\mu_B a_h)$, respectively.

The stationary state of the monopole is obtained by using the standard imaginary-time propagation combined with finite-difference methods [54–56]. Equations (2)–(4) are solved by using the second-order centered finite difference for the spatial discretization and the backward and forward Euler schemes of the linear and nonlinear terms for the time discretization. The average energy decays monotonically with time until the steady states are reached. The computational grids are $120 \times 120 \times 120$, corresponding to the volume being $20 \times 20 \times 20 \, (a_h^3)$ or $34.2 \times 34.2 \times 34.2 \, (\mu\text{m}^3)$. The final steady state is independent of the initial trial wave function. The trial wave function is given by the normalized random number of complex values. The dynamic evolution is obtained

by using the split-operator Crank-Nicolson method with the time stepping being $10^{-4}/\omega$.

We first study the structures of the monopoles in the absence of the SO coupling, as seen in Appendix B. To our knowledge, the homogeneous bias field is a necessary condition for observing the monopole creation process [9,15]. However, our emphasis is to investigate the final steady state of the monopole, not the creation process of the monopole. Therefore, the homogeneous bias field is not a necessary condition in the present work and therefore is not included in our model. In this case, the vortex line corresponding to the monopole will not be along the symmetry axis of the system [15]. Therefore, the doubly quantized vortex line attached to the monopole shows a branchlike distribution, splitting into two singly quantized vortex lines partially in the $m_F = +1$ and -1 components.

When the SO coupling is weak, the monopoles with the polar-core vortex are found, as shown in Fig. 1. The structure of the monopoles with the polar-core vortex represents a single vortex line in the $m_F = +1$ component, a soliton in the $m_F = 0$ component, and a single antivortex line in the $m_F = -1$ component. Compared with the monopoles in BECs without the SO coupling [9,15], in the present system there exist two monopoles that locate at the endpoints of two nodal lines along the vertical axis [as highlighted by the red arrows in Fig. 1(b)], which is caused by the coupling between the spin and the center-of-mass motion of the atom. In addition, we study the dynamics of the monopoles with the polar-core vortex and the dynamics of the monopoles when the quadrupole field is turned off (for details see Appendixes E and F). We further discuss the influence of the anisotropic optical trap and the magnetic field gradient on the monopoles [for details see Appendix C].

Next we investigate the influence of the interaction on the morphology of the monopoles. As shown in Fig. 2, the monopole with a Mermin-Ho vortex [57] is obtained for a smaller λ_2 value. The monopole with a Mermin-Ho vortex represents a soliton in the $m_F = +1$ component, a single vortex line in the $m_F = 0$ component, and a double quantized vortex line in the $m_F = -1$ component. In previous study, the monopole with a Mermin-Ho vortex has been observed in spinor BECs with a synthetic magnetic field [9]. Figure 2 confirms that the monopole with a Mermin-Ho vortex can also exist in the condensates with the SO coupling.

III. DIRAC MONOPOLES WITH SQUARE LATTICE

The monopoles with the square lattice are found as the SO coupling strength increases, as shown in Fig. 3. The square lattice is observed in the central region of the BECs. Meanwhile, the density distribution in the longitudinal direction is of the stripe structure. The phases at both sides of the $x = 0$ and $y = 0$ slice planes are inverse for all spin components. The morphology of the monopole with the square lattice is not affected by the interactions, because the corresponding lowest-energy state is actually not affected by the interactions when the SO coupling is strong. Finally, we also briefly discuss the influence of the anisotropic SO coupling on the structure of the monopole. The monopole may be canceled because the Dirac strings are removed in the case of anisotropic SO coupling, as shown in Appendix D.
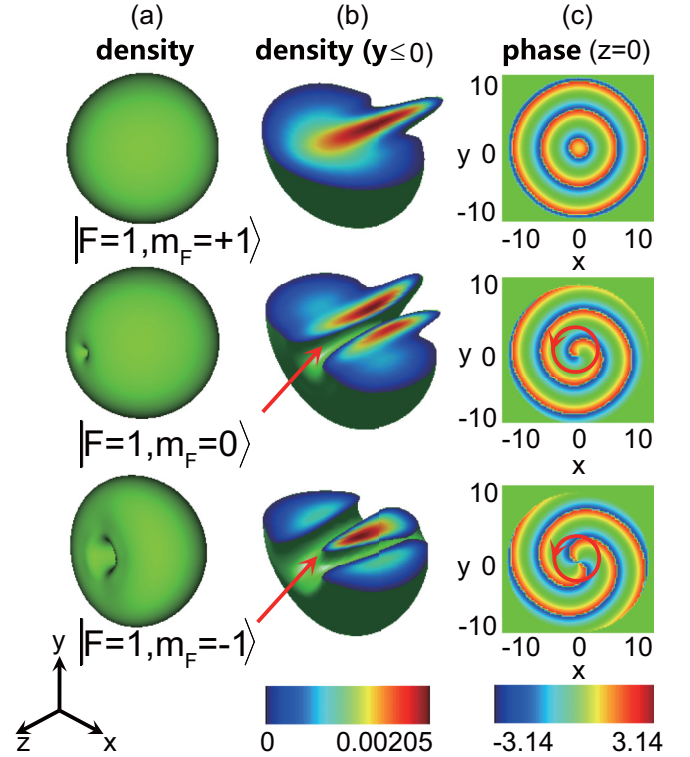

FIG. 2. The monopoles with the Mermin-Ho vortex. (a) Isosurface of particle densities. (b) Segments of isosurface of particle densities ($y \leqslant 0$). The position of the nodal line (Dirac string) is highlighted by the red arrow. (c) Phase distributions in the $z = 0$ planes. The single vortex ($m_F = 0$) and double vortex ($m_F = -1$) have the same circulations, as highlighted by the red circles. The simulation uses $\lambda_2 = -15$ and $\kappa = 2$ with the other parameters being the same as the ones in Fig. 1.

The spinor BECs can be considered as a magnetic system, which can reflect physical properties of topological defects [53]. We study topological spin textures of the monopoles. The components of the spin vector are given by $F_x = [\psi_1^* \psi_0 + \psi_0^*(\psi_1 + \psi_{-1}) + \psi_{-1}^* \psi_0]/\sqrt{2}$, $F_y = i[-\psi_1^* \psi_0 + \psi_0^*(\psi_1 - \psi_{-1}) + \psi_{-1}^* \psi_0]/\sqrt{2}$, and $F_z = |\psi_1|^2 - |\psi_{-1}|^2$ [42,43,57–61]. The spin textures of the monopoles with the polar-core vortex are shown in Fig. 4(a). The spin aligns with the radially inward hedgehog distribution in the x-y plane, representing the spin texture of a south magnetic pole, while the spin textures in the x-z and y-z planes show the cross-hyperbolic distribution [58,62]. Compared with the case without the SO coupling [24], in our case the SO coupling changes the spin direction, which causes the north magnetic pole to transform into the south magnetic pole. As shown in Fig. 4(b), the spin textures of the antimonopoles represent the north magnetic poles. For the case of the strong SO coupling [see Fig. 4(c)], the spin textures are divided into four portions in the x-y plane, which behaves as the ferromagnetic distribution at each portion. The spin orientations at two diagonal portions are opposite, which indicates the structures of monopoles and antimonopoles that locate in the boundaries of the condensates. The spin textures in the x-z and y-z planes form the spin stripe. The dynamic evolution of the spin texture is shown in Fig. 14
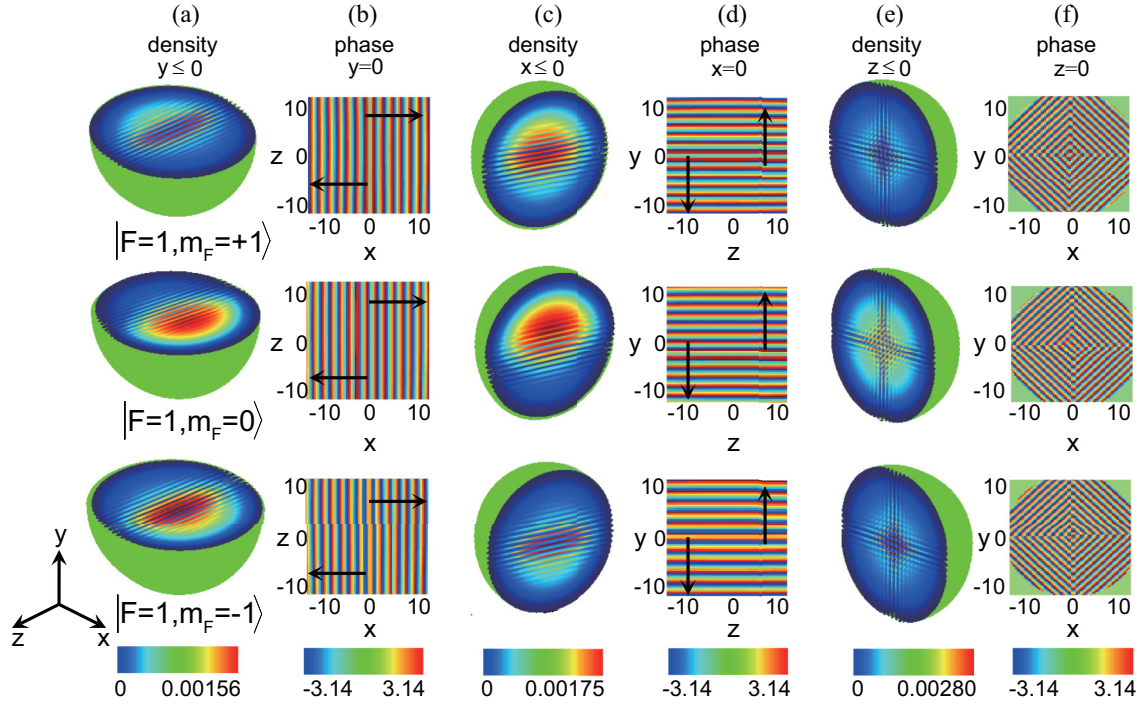
FIG. 3. The monopoles with the square lattice. (a), (c), and (e) Particle densities for $y \leqslant 0$, $x \leqslant 0$, and $z \leqslant 0$. (b), (d), and (f) Phase distributions in the $y = 0$, $x = 0$, and $z = 0$ planes. The phases at both sides of the $y = 0$ and $x = 0$ planes are inverse, as highlighted by the black arrows. The simulation uses $\kappa = 16$ with the other parameters being the same as the ones in Fig. 1.

in Appendix G, which further proves that the monopoles with the polar-core vortex are stable.

IV. PHASE DIAGRAM AND EXPERIMENTAL PROTOCOL

The interplay between the SO coupling and the interaction leads to the rich phase diagrams of the monopoles. Figure 5(a) shows the phase diagram of the monopole structure as functions of κ and λ_0 for $\lambda_2 = -75$. The monopole is metastable when κ is less than a critical value $\kappa_c = 0.8$. The corresponding monopole structure is the same as the monopole structure when $\kappa = 0$, as shown in Fig. 7 in Appendix B. For $0.8 < \kappa \leqslant 3$, the monopoles with the polar-core vortex exist when $0 < \lambda_0 \leqslant 3000$ and $5000 < \lambda_0 \leqslant 8000$, while the monopoles with the Mermin-Ho vortex emerge when $3000 < \lambda_0 \leqslant 5000$ and $8000 < \lambda_0 \leqslant 11\,000$. Because the spin-independent interaction causes the variation of the local magnetic order, a cyclic phase transition from Dirac monopoles with a polar-core vortex to those with a Mermin-Ho vortex can occur as the increasing λ_0. The monopoles with the square lattice appear when $\kappa > 3$, confirming that the monopoles are not affected by the interactions and are able to exist in the wide parameter region for the case of the strong SO coupling. Figure 5(b) shows the phase diagram of the monopole structure as functions of κ and λ_2 for $\lambda_0 = 7500$. The obtained monopole is metastable for $\kappa \leqslant 0.8$, where the monopole structure is the same as the structure when $\kappa = 0$. For $0.8 < \kappa \leqslant 3$, there exist the monopoles with the Mermin-Ho vortex when $\lambda_2 < 60$, while the monopoles with the polar-core vortex emerge when $\lambda_2 > 60$. Increasing λ_2 leads to the direct phase transition from the monopoles with the Mermin-Ho vortex to the monopoles with the polar-core vortex.

Finally, we discuss the experimental feasibility of creating the monopoles in SO coupled BECs in Appendix A. We consider spin-1 BECs of alkali ^{87}Rb atoms, where particle number $N \approx 0.6(1.8) \times 10^5$. First, a quadrupole field realized by a pair of Helmholtz coils is turned on. The strength of the magnetic field is zero at the center of the quandrupole field, which corresponds to a point source of the superfluid flow. Afterward, when the formed point source of the superfluid flow is stable [15], the quadrupole field is turned off. At the same time, the pulsed magnetic fields are utilized to produce two-dimensional SO coupling [38]. We take some parameters from the recent experiments [9,15,38], including the isotropic optical trap $\omega_r = \omega_z = 2\pi \times 250$ Hz, the anisotropic optical trap $\omega_r = 2\pi \times 160Z$ Hz and $\omega_z = 2\pi \times 220$ Hz, the constant bias magnetic field $B^{(0)} = 20$ G, and the quadrupole field gradient $B'_1 = 0.03 - 0.1$ T/m. In the case of the monopoles with the polar-core vortex, the SO coupling strength $\kappa \sim 0.8 - 3$. We find the dynamic period of the monopoles with the polar-core vortex $t' \sim 11$ ms, which can be stably observed in experiments.

V. CONCLUSION

We have shown that the weak SO coupling leads to the emergence of monopoles with the polar-core vortex that are long-lived, and the strong SO coupling leads to the emergence of monopoles with the square lattice in spinor BECs. We have predicted the rich phase diagrams of the monopoles by changing the SO coupling strength, the spin-dependent interaction, and the spin-independent interaction. The influence of the anisotropic SO coupling, the anisotropic optical trap, and the magnetic field gradient on the properties of the monopoles have
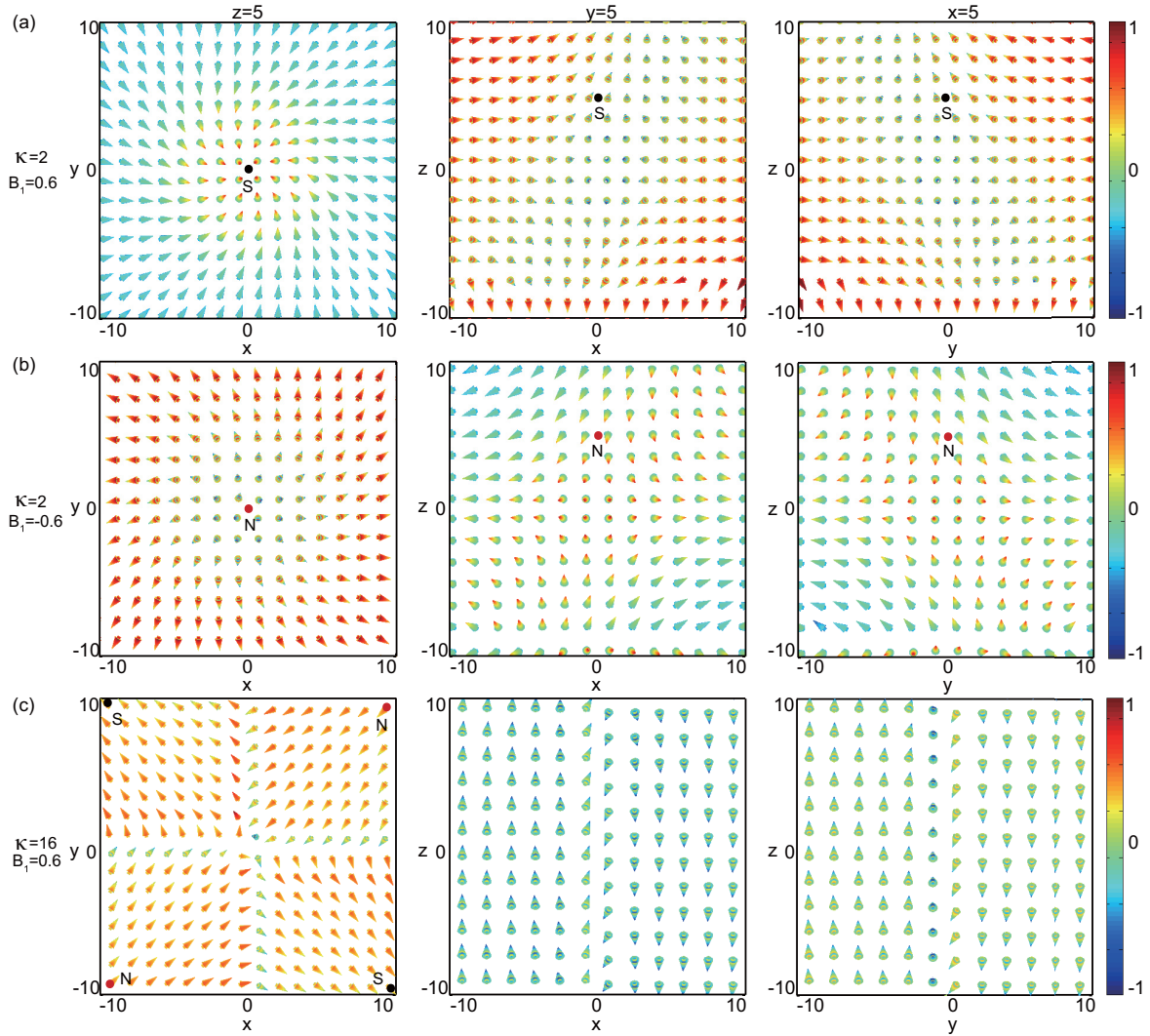
FIG. 4. (a) Spin textures of monopoles with the polar-core vortex describe the south magnetic poles (the black dot S). (b) Spin textures of the antimonopoles describe the north magnetic poles (the red dot N). (c) Spin textures of the monopoles with the square lattice. The other parameters are the same as the ones in Fig. 1.

also been investigated. We provide an experimental scheme to observe these monopoles as well, which can be proved by

means of imaging the vortex lines. This work paves the way for future explorations of the monopole with respect to gauge field, topological defects, and the corresponding dynamical stability in quantum systems.
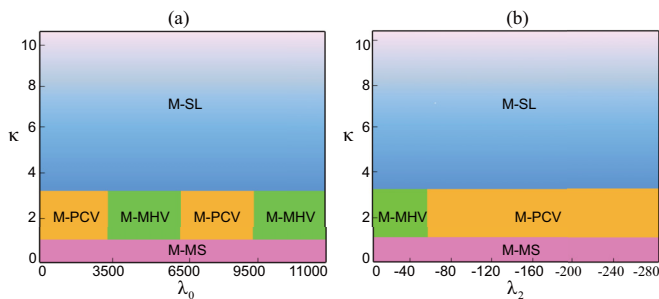
FIG. 5. (a) Phase diagram of the monopole with the SO coupling strength κ and spin-independent interaction parameter λ_0 for a given spin-dependent interaction parameter λ_2. (b) Phase diagram of the monopole with κ and λ_2 for a given λ_0. Four phases are identified, including the metastable monopoles (M-MS), the monopoles with the polar-core vortex (M-PCV), the monopoles with the Mermin-Ho vortex (M-MHV), and the monopoles with the square lattice (M-SL).

APPENDIX A: EXPERIMENTAL SETUP OF CREATING THE MONOPOLES IN SPIN-ORBIT COUPLED BOSE-EINSTEIN CONDENSATES

The experimental setup is shown schematically in Fig. 6(a). We consider spin-1 BECs of alkali ^{87}Rb atoms, where the ^{87}Rb BECs contain about $N \approx 0.6(1.8) \times 10^5$ atoms. First, a
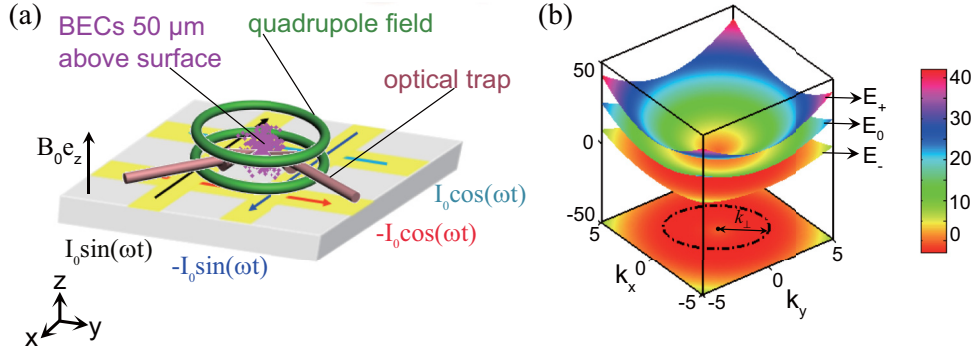
FIG. 6. Experimental setup of creating the monopoles in SO coupled BECs. (a) Experimental geometry of creating the quadrupole field and the SO coupling. A pair of Helmholtz coils are used for creating the quadrupole fields, where the pink particles represent ^{87}Rb atoms and the kermesinus arrows show beam paths of the optical trap. The pulsed magnetic field is used for creating the SO coupling, where the cloud of atoms is located $50\,\mu$m above the surface of an atom chip. A bias field B_0 along the z axis induces the magnetic splitting. Two pairs of parallel microwires are embedded in the atom chip, which produces the amplitude modulated rf field along the x and y axis, respectively. These two effective coupling vectors in the x-y plane induce effective two-dimensional SO coupling in the first-order approximation to short enough duration. (b) Energy spectrum. The single-particle energy spectrum of the monopole with SO coupling strength $\kappa = 2$ in the k_x-k_y plane is divided into three branches E_+, E_0, and E_-, and the black circular ring represents the Rashba ring from the minimum energy spectrum.

quadrupole field is applied and turned on, which is realized by a pair of Helmholtz coils with oppositely circulating currents. The strength of the magnetic field is zero at the center of the quandrupole field, which corresponds to a point source of the superfluid flow. The superfluid flow of the spinor condensates can be characterized by its vorticity $\Omega_s = \hbar\hat{\mathbf{e}}_{r'}/(mr'^2)$, where
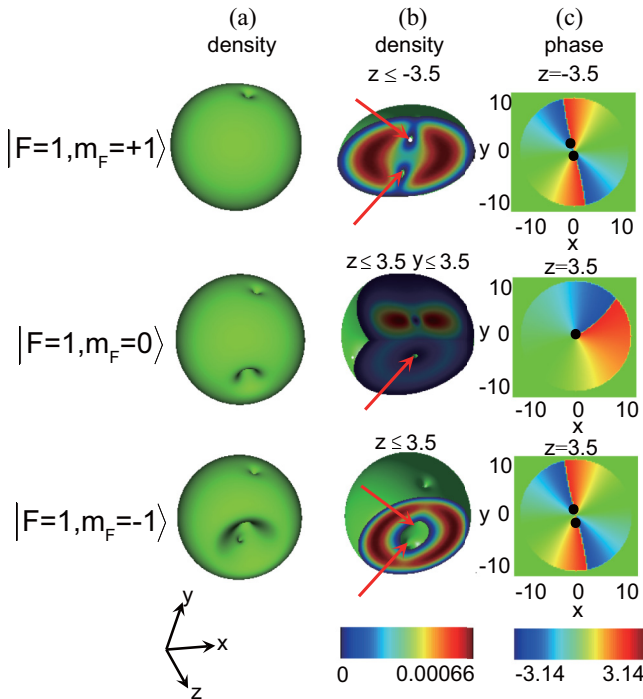

FIG. 7. (a) Isosurface of particle densities. (b) Segments of the isosurface of particle densities. (c) Phase distributions of slice planes. The black dots indicate the locations of vortices. The monopole is metastable, and a double vortex line has split into two single vortex lines partially, as highlighted by the red arrows. The simulation uses $\kappa = 0$, and the other parameters used in numerical calculation are the same as the ones in Fig. 1.

r' is the sphere radius. The vorticity Ω_s is equivalent to the magnetic field of a monopole that distributes radially outward in a hedgehog form. Therefore, a monopole can be considered as a point source of the superfluid flow [15]. In experiments, due to the fluctuating background fields and mechanical instabilities in the optical trap, the point source may be drifted to outside of the condensates. In order to avoid the occurrence of such phenomenon, we make the point source stay inside the condensates by controlling and adjusting the strength of the magnetic field gradient. When a point source of the superfluid flow is stably formed, the quadrupole field is turned off. Subsequently, the pulsed magnetic fields are utilized to create two-dimensional spin-orbit (SO) coupling [38]. The cloud of atoms is situated $50\,\mu$m above the surface of the atom chip. A constant bias magnetic field $B^{(0)}\mathbf{e}_z$ is applied out of plane, which leads to splitting of the magnetic sublevels. Two pairs of microwires parallel to $\mathbf{e}_x$ and $\mathbf{e}_y$ provide the rf magnetic fields $\mathbf{B}_x(\mathbf{r},t)$ and $\mathbf{B}_y(\mathbf{r},t)$. In the first stage $(0 \leqslant t < \tau)$, the rf magnetic field $\mathbf{B}_x(\mathbf{r},t)$ with the frequency ω_1 leads to an effective coupling vector in the x direction and a spin-dependent phase gradient in the y direction, where the SO coupling is written as $-i\hbar\kappa_x\mathcal{F}_x\partial_x$. In the second stage $(\tau \leqslant t < 2\tau)$, the rf magnetic field $\mathbf{B}_y(\mathbf{r},t)$ with frequency ω_2 leads to an effective coupling vector in the y direction and a spin-dependent phase gradient in the x direction, where the SO coupling is written as $-i\hbar\kappa_y\mathcal{F}_y\partial_y$. When both rf magnetic fields $\mathbf{B}_x(\mathbf{r},t)$ and $\mathbf{B}_y(\mathbf{r},t)$ are applied, the two-dimensional SO coupling is created, which is written as $\mathcal{V}_{so} = -i\hbar(\kappa_x\mathcal{F}_x\partial_x + \kappa_y\mathcal{F}_y\partial_y)$ in the first-order approximation for a sufficiently short duration τ. The strengths of the SO coupling κ_x and κ_y are determined by the strengths of the magnetic field gradient of $\mathbf{B}_x(\mathbf{r},t)$ and $\mathbf{B}_y(\mathbf{r},t)$. Due to the SO coupling, the spin degeneracy of three-component bosons is lifted. The free particle energy spectrum splits into three energy branches with the different helicities [see Fig. 6(b)]. The Rashba ring can be seen from the minimum energy spectrum, as denoted by the black circular ring in Fig. 6(b). Some simulated parameters are taken from the recent experiments [9,15,38]. The isotropic
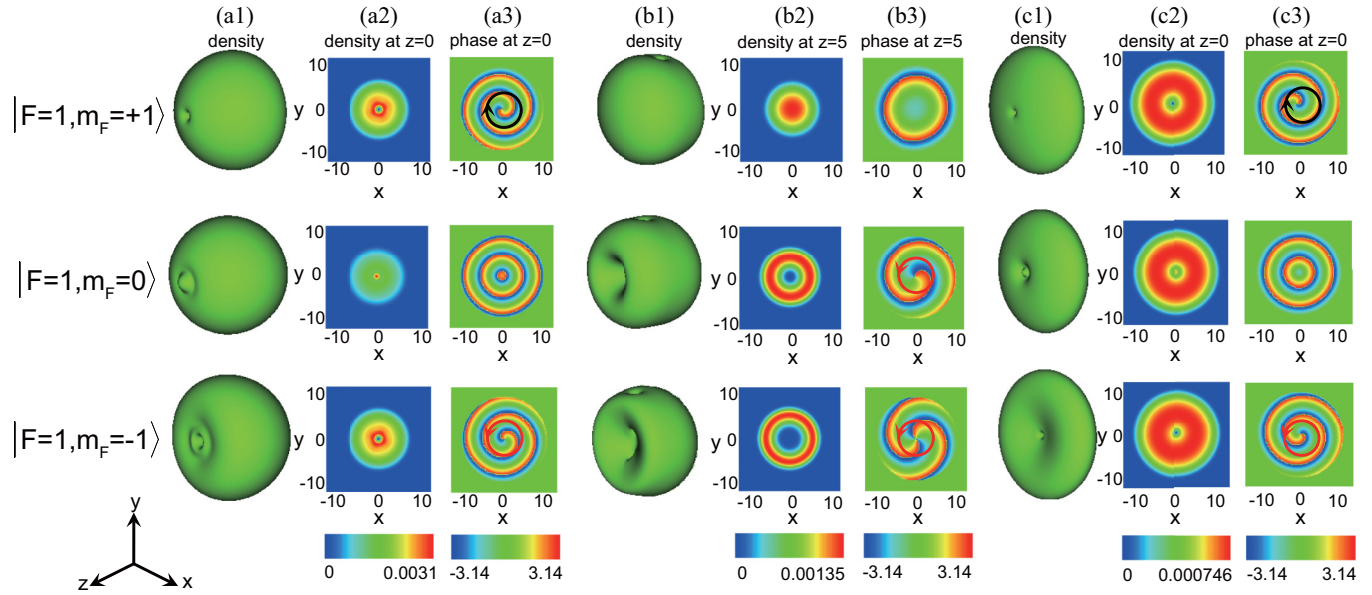
FIG. 8. (a1), (b1), and (c1) The isosurface of particle densities. (a2), (b2), and (c2) The particle densities of the slice planes. (a3), (b3), and (c3) The phase distributions of the slice planes, where the vortex and antivortex are highlighted by the black and red circles, respectively. The simulation uses $\kappa = 2$, $\lambda_2 = -75$, $B_1 = 0.6$, and $\lambda_0 = 7500$.

optical trap $\omega_r = \omega_z = 2\pi \times 250$ Hz, the anisotropic optical trap $\omega_r = 2\pi \times 160$ Hz and $\omega_z = 2\pi \times 220$ Hz, the constant bias magnetic field $B^{(0)} = 20$ G, and the quadrupole field gradient $B_1' = 0.03 - 0.1$ T/m.

APPENDIX B: STRUCTURES OF THE MONOPOLES IN THE ABSENCE OF THE SPIN-ORBIT COUPLING

Figure 7 shows the result of the monopoles in the absence of the SO coupling. To our knowledge, the homogeneous bias field is a necessary condition for observing the monopole creation process [9,15]. However, our emphasis is to investigate the final steady state of the monopole, not the creation process of the monopole. Therefore, the homogeneous bias field is not a necessary condition in the present work and therefore is not included in our model. In this case, the vortex line corresponding to the monopole will not be along the symmetry axis of the system [15]. In addition, due to a doubly quantized vortex line, it is expected to be prone to splitting into two vortex lines each carrying one angular momentum quantum. Therefore, the doubly quantized vortex line attached to the monopole shows a branchlike distribution, splitting into two singly quantized vortex lines partially in the $m_F = +1$ and -1 components [as highlighted by the red arrow in Fig. 7(b)].
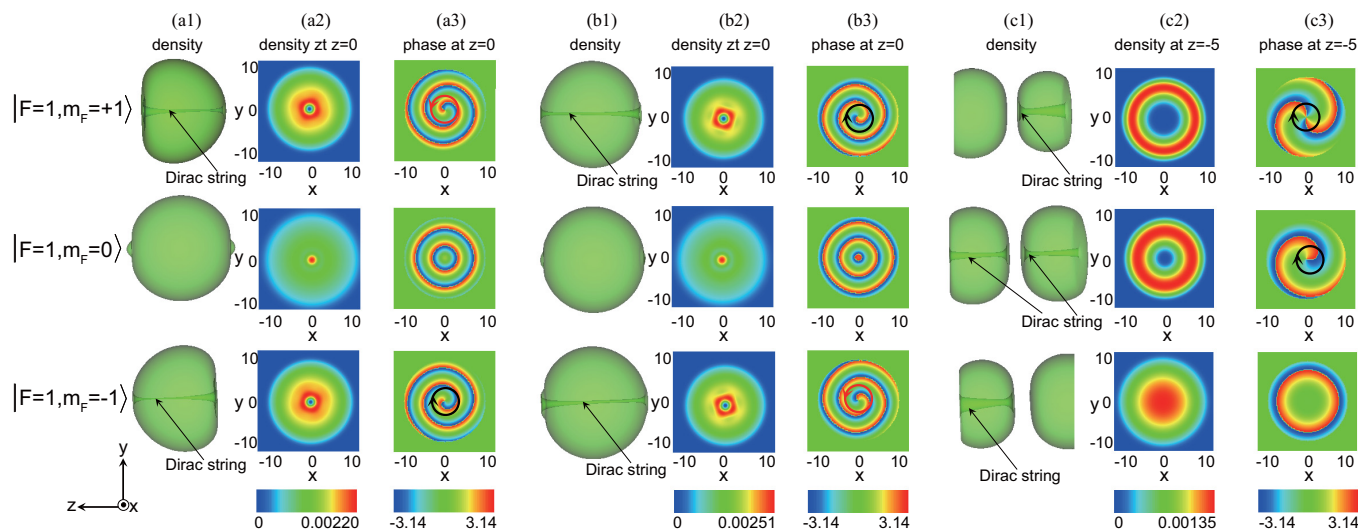

FIG. 9. (a1), (b1), and (c1) The isosurface of the particle densities, Dirac strings are denoted by the black arrows. (a2), (b2), and (c2) The particle densities of the slice planes. (a3), (b3), and (c3) The phase distributions of the slice planes. The vortex and antivortex are highlighted by the black and red circles, respectively. The strength of the magnetic field gradient is taken to be $B_1 = -0.6$ for (a1)–(a3), $B_1 = 0.2$ for (b1)–(b3), and $B_1 = 3.8$ for (c1)–(c3). The simulation uses $\kappa = 2$, $\lambda_2 = -75$, $\lambda_0 = 7500$, and $\omega_r = \omega_z = 2\pi \times 250$ Hz.
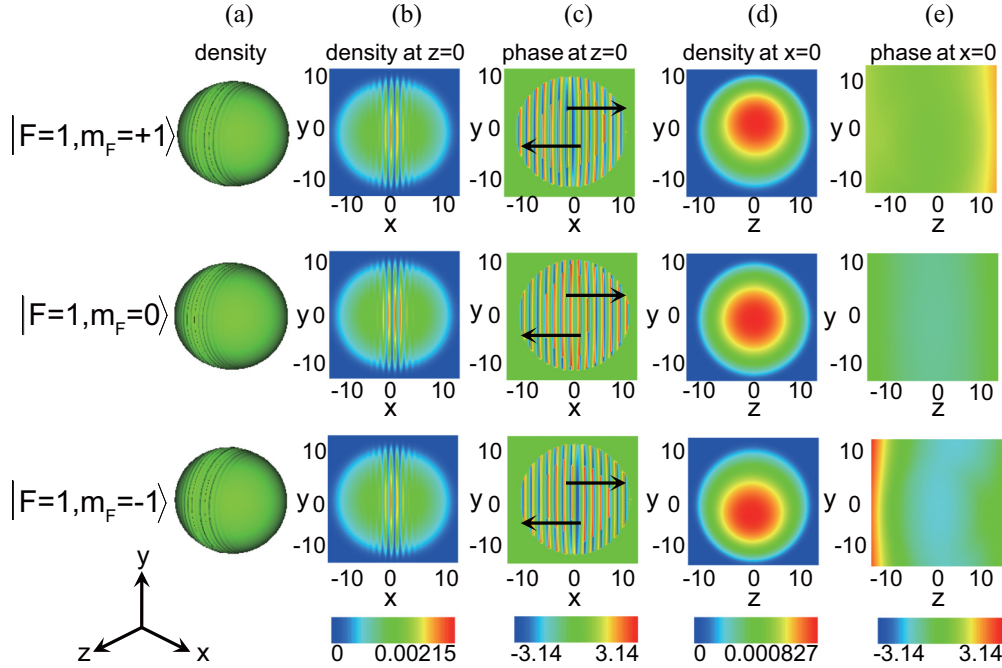
FIG. 10. (a) Isosurface of particle densities. (b) and (c) Densities and phase distributions in the $z = 0$ planes. The phenomena in the x-z plane are similar to those in the x-y plane. In (c), the phases at both sides of the $z = 0$ slice plane are inverse, which is highlighted by the black arrow. (d) and (e) Densities and phase distributions in the $x = 0$ planes. The simulation uses the anisotropic SO coupling $\kappa_x = 8$ and $\kappa_y = 2$, $\lambda_2 = -75$, $\lambda_0 = 7500$, $B_1 = 0.6$, and $\omega_r = \omega_z = 2\pi \times 250$ Hz.

The vortex lines for the $m_F = +1$ component locate in the part of $z < 0$. The vortex lines for the $m_F = -1$ component locate in the part of $z > 0$. These vortex lines extend along the $\pm y$ directions to the boundary of the BECs. The phases at both sides of the vortex line are the same. For the case of the $m_F = 0$ component, the two vortex lines in the $x = 0$ plane cross each other and topologically invariant winding number is 1. The phases of the vortex line along the z and y axes are opposed, being similar to the vortex-antivortex pair [63,64]. In fact, the doubly quantized vortex will split into two separated singly quantized vortices gradually as time goes on [65,66]. Therefore, Fig. 7 indicates that the monopole is metastable in the absence of the SO coupling.

APPENDIX C: EFFECTS OF THE ANISOTROPIC OPTICAL TRAP AND THE QUADRUPOLE FIELD GRADIENT ON THE MONOPOLES

In this section, we investigate the monopole structures for an anisotropic optical trap. For comparison, we first consider the isotropic optical trap with $\omega_r = \omega_z = 2\pi \times 250$ Hz [15], as shown in Figs. 8(a1)–8(a3). The monopoles with the polar-core vortex are obtained, which represents a single vortex line in the $m_F = +1$ component, a soliton in the $m_F = 0$ component, and a single antivortex line in the $m_F = -1$ component. In Figs. 8(b1)–8(b3), the trapping frequencies are given by $\omega_r = 2\pi \times 160$ Hz and $\omega_z = 2\pi \times 220$ Hz [9], and the anisotropy parameters of the optical trap are given by $\gamma_r = 1$ and $\gamma_z = 1.375$. The Dirac string embedded in the BECs splits into two strings with a singly quantized vortex. In this case, the result indicates that this anisotropic trapping potential leads to the metastable monopole. In fact, the monopoles with the

polar-core vortex exist in the condensates when the anisotropy of the optical trap is less than the magnitude of $\gamma_r = 1$ and $\gamma_z = 1.375$. In Figs. 8(c1)–8(c3), the trapping frequencies are given by $\omega_r = 2\pi \times 160$ Hz and $\omega_z = 2\pi \times 320$ Hz, and the anisotropy parameters of the optical trap are given by $\gamma_r = 1$ and $\gamma_z = 2$. The monopoles with the polar-core vortex continue to exist in the BECs. Therefore, Fig. 8 confirms that the monopoles with the polar-core vortex can also occur in the presence of the oblate trap.

The external magnetic fields affect the positions of Dirac strings and the spin direction [24]. In Fig. 9 we investigate the influence of the quadrupole field gradient on the monopoles. In Figs. 9(a1)–9(a3), when the strength of the quadrupole field gradient is negative, such as $B_1 = -0.6$, the antimonopoles emerge in the system. The structures of the antimonopoles represent a singly antivortex line in the $m_F = +1$ component, a soliton in the $m_F = 0$ component, and a single vortex line in the $m_F = -1$ component, which is caused by the exchange of the vortex lines between the $m_F = +1$ component and the $m_F = -1$ component. In this case, the antimonopole stucture essentially represents the polar-core vortex, while the charge corresponding to the antimonopole is the north magnetic pole [see Fig. 4(b)]. In Figs. 9(b1)–9(b3), when the strength of the quadrupole field gradient is positive, such as $B_1 = 0.2$, the corresponding monopole structure is similar to the monopole structure obtained for $B_1 = 0.6$, which represents a single vortex line in the $m_F = 1$ component, a soliton in the $m_F = 0$ component, and a single antivortex line in the $m_F = -1$ component. In Figs. 9(c1)–9(c3), when B_1 is increased, such as $B_1 = 3.8$, the atomic cloud expands along the $\pm z$ direction, because increasing B_1 results in stronger magnetic forces [9]. The atoms are difficult to be bounded in the central region of
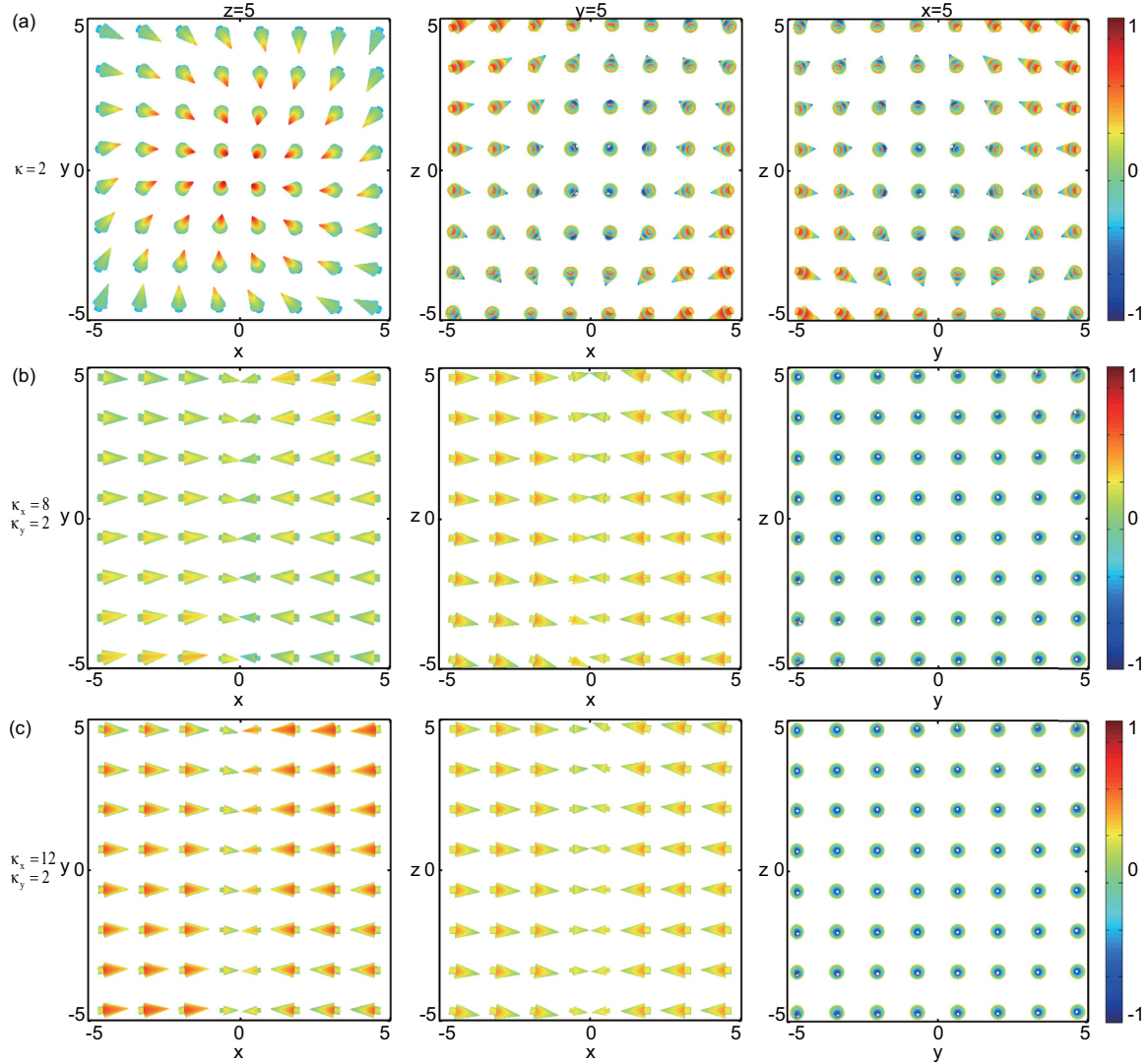
FIG. 11. (a) When the SO coupling $\kappa_x = \kappa_y = \kappa = 2$, we obtain the spin textures of the monopoles with the polar-core vortex in the slice planes of $z = 5$, $y = 5$, and $x = 5$. (b) When the SO coupling $\kappa_x = 8$ and $\kappa_y = 2$, the spin textures show the stripe distribution in the $z = 5$ and $y = 5$ planes and the plane wave ferromagnetic distribution in the $x = 5$ plane. (c) When the SO coupling $\kappa_x = 12$ and $\kappa_y = 2$, the spin textures are similar to those in (b). The simulation uses $B_1 = 0.6$, $\lambda_2 = -75$, $\lambda_0 = 7500$, and $\omega_r = \omega_z = 2\pi \times 250\,\mathrm{Hz}$.

trap when the strength of the magnetic field gradient is strong. A vortex line is terminated in the middle of the atomic cloud for the $m_F = +1$ and $m_F = -1$ components, and the phase winding of the vortex line is 4π between the $m_F = +1$ and $m_F = -1$ component. In addition, for the $m_F = 0$ component, the vortex line locates in the positive and negative z axis, and the corresponding phase winding number of the vortex line is 1.

APPENDIX D: GROUND STATES FOR THE ANISOTROPIC SPIN-ORBIT COUPLING

In Fig. 10 we briefly discuss the case of the anisotropic SO coupling, where the SO coupling strength is strong in the x direction with $\kappa_x = 8$, but is weak in the y direction with $\kappa_y = 2$. The result shows that the monopole may be canceled, as the anisotropic SO coupling can remove the Dirac string. Instead, the condensate splits into many segments along the x direction, representing a stripe distribution along the x direction and a plane wave distribution in the y-z plane. The

phases along the x direction are inverse, as shown in Fig. 10(c). The spin textures of the spinor BECs for the anisotropic SO coupling are shown in Fig. 11. For comparison, when the SO coupling is isotropic, such as $\kappa = 2$, the spin aligns with the radially inward hedgehog distribution in the x-y plane, while the spin textures in the x-z and y-z planes show the cross-hyperbolic distribution [see Fig. 11(a)]. When the SO coupling is anisotropic, such as $\kappa_x = 8$ and $\kappa_y = 2$, the spin textures in the x-y plane are the same as ones in the x-z plane, and the spin textures in the y-z plane show the ferromagnetic distribution [see Fig. 11(b)]. Meanwhile, for the x-y and x-z planes, the spin distribution is the same in the y and z directions but is contrary in the x direction. Furthermore, as the anisotropy of the SO coupling is increased, for example, $\kappa_x = 12$ and $\kappa_y = 2$ [see Fig. 11(c)], we find that the spin textures are similar to the spin textures shown in Fig. 11(b). This indicates that the spin textures are independent of the strength of the anisotropic SO coupling.
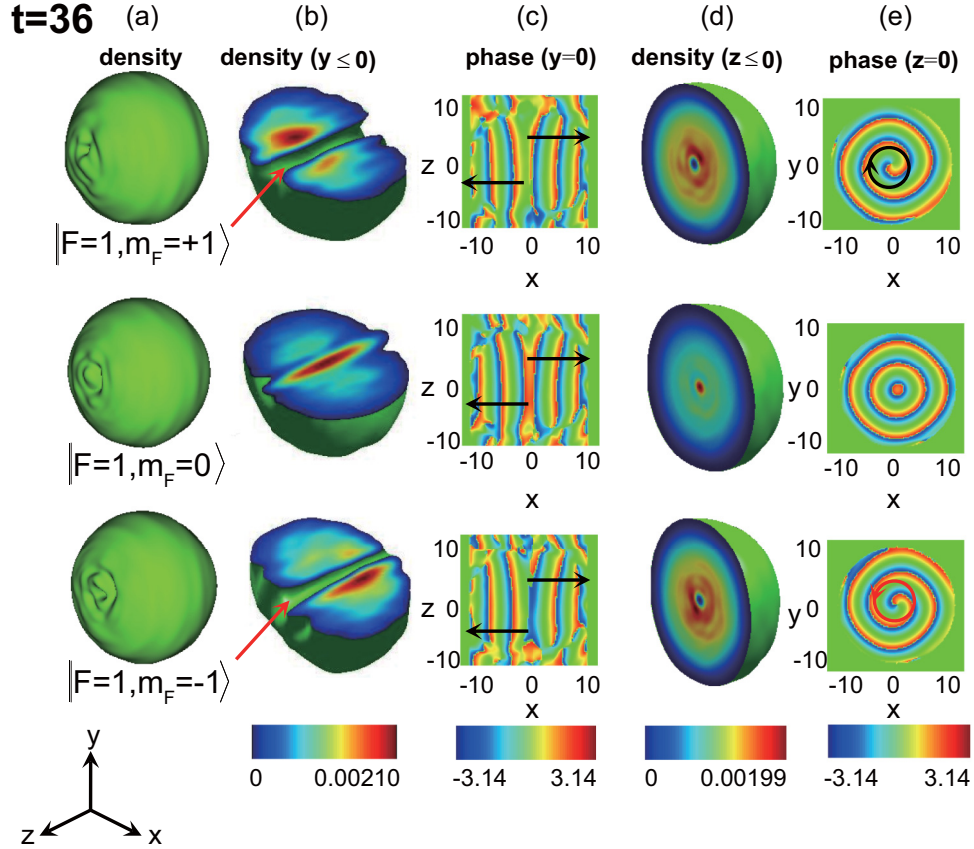
FIG. 12. Real-time evolutions of monopoles with the polar-core vortex. (a) Isosurface of particle densities. (b) Particle densities for $y \leqslant 0$, where the red arrow highlights the nodal line (Dirac string). (c) Phase distributions in the $y = 0$ planes. The phases at both sides of the $y = 0$ planes are inverse, which is highlighted by the black arrow. (d) Particle densities for $z \leqslant 0$. (e) Phase distributions in the $z = 0$ planes; the single vortex and antivortex are highlighted by the black and red circles, respectively. The simulation parameters are the same as the ones in Fig. 1, and the real time $t' = 0.64t$ ms.
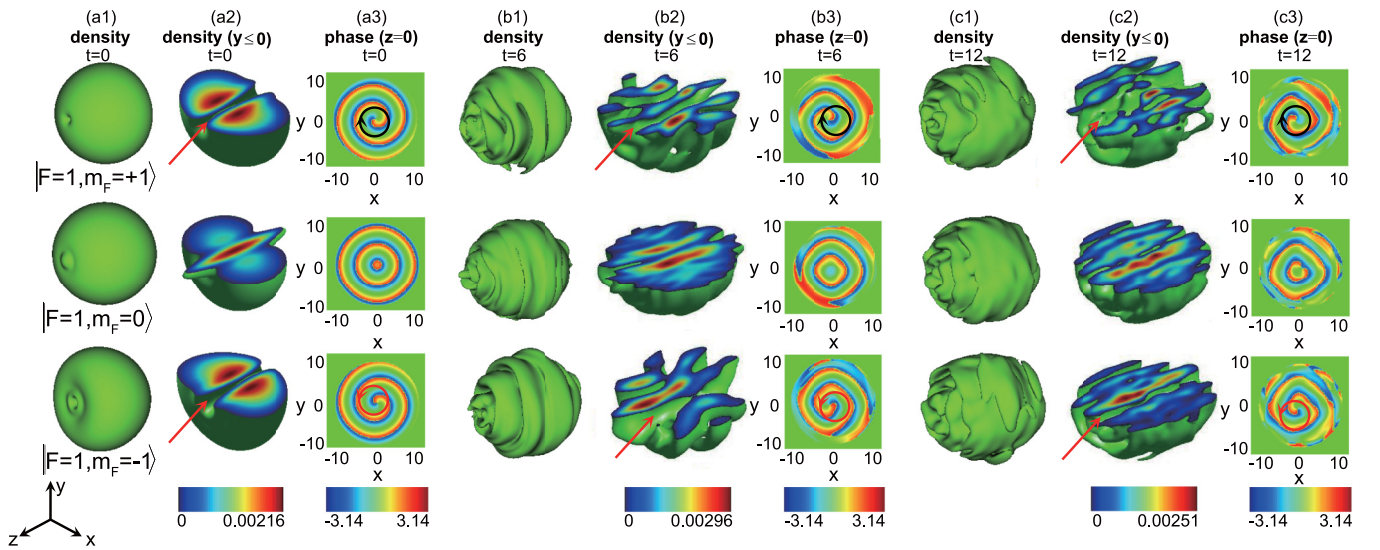

FIG. 13. The monopoles with the polar-core vortex remain stable even when the quadrupole field is turned off. (a1)–(a3) $t = 0$, (b1)–(b3) $t = 6$, and (c1)–(c3) $t = 12$. (a1), (b1), and (c1) Isosurface of particle densities. (a2), (b2), and (c2) Particle densities for $y \leqslant 0$. The red arrow denotes the location of the nodal line (Dirac string). (a3), (b3), and (c3) Phase distributions in the $z = 0$ planes. The single vortex and antivortex are highlighted by the black and red circles, respectively. The simulation uses $\kappa = 2$, $\lambda_2 = -75$, $\lambda_0 = 7500$, and $\omega_r = \omega_z = 2\pi \times 250$ Hz. The real time $t' = 0.64t$ ms.
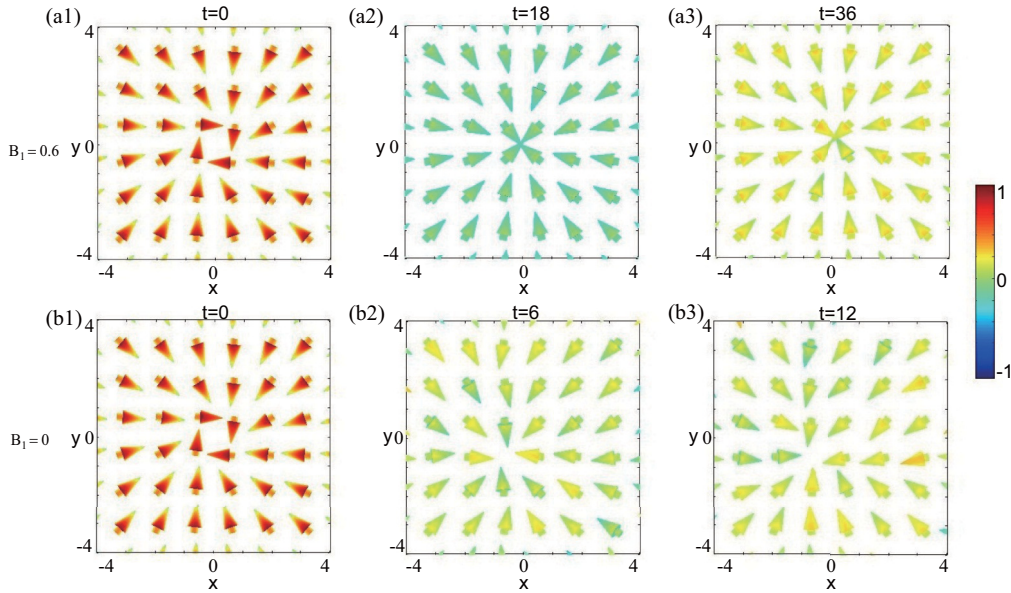
FIG. 14. (a1)–(a3) Dynamic evolution of the spin texture of the monopoles with the polar-core vortex for the x-y plane in the presence of the quadrupole field, where $B_1 = 0.6$, $\kappa = 2$, $\lambda_2 = -75$, $\lambda_0 = 7500$, $\omega_r = \omega_z = 2\pi \times 250$ Hz, and the real time $t' = 0.64t$ ms. (a1) $t = 0$, (a2) $t = 18$, and (a3) $t = 36$. (b1)–(b3) Dynamic evolution of the spin texture of the monopoles with the polar-core vortex for the x-y plane when the quadrupole field is turned off, where $B_1 = 0$ and the other parameters are the same as those in (a1)–(a3). (b1) $t = 0$, (b2) $t = 6$, and (b3) $t = 12$.

APPENDIX E: DYNAMIC EVOLUTION OF THE MONOPOLES WITH THE POLAR-CORE VORTEX

We simulate the dynamic evolution of the monopoles with the polar-core vortex in order to investigate the stability of the monopoles with the polar-core vortex. Figure 12 shows the morphology of the monopoles with the polar-core vortex when $t = 36$ corresponding to the real time $t' = 23$ ms. The nodal line corresponding to monopole is very stable during the dynamic evolution, as highlighted by the red arrows in Fig. 12(b). Moreover, the phase profile of the wave function in the $z = 0$ plane shows that the singly vorticity is well maintained, and no vortex splitting is observed during the dynamic evolution [see Fig. 12(e)]. The nodal lines corresponding to the monopoles with the polar-core vortex are in contrast to the nodal lines observed in the absence of the SO coupling that were unstable to decay after only only 10 ms [9]. The stable morphology of the monopoles with the polar-core vortex is well kept in our whole simulation time window. The monopole structures at the different times will be discussed in Fig. 15 in Appendix G.

APPENDIX F: DYNAMIC EVOLUTION OF THE MONOPOLES IN THE ABSENCE OF THE QUADRUPOLE FIELD

In this section, we further discuss the dynamics of the monopole structure in the absence of the quadrupole field. The initial states of the monopoles are shown in Figs. 13(a1)–13(a3). The evolution of the monopole structure has been simulated for $t = 6$ and $t = 12$ with a time step $10^{-4}/\omega$ [see Figs. 13(b1)–13(c3)]. During the time evolution, the isosurface of density becomes rough, as shown in Figs. 13(b1) and 13(c1). The Dirac strings still exist in the condensates, which

is highlighted by the red arrow in Figs. 13(b2) and 13(c2). Furthermore, as seen in the phase profile of the wave function, the singly quantized vortex and antivortex are stable against splitting, which are highlighted by the black and red circles, as shown in Figs. 13(b3) and 13(c3). In previous work [24], the Dirac strings were observed to expand at about $t = 8$ ($t' = 5.12$ ms) when the quadrupole field is turned off. In the present work, the Dirac strings are not observed to expand until a longer time such as $t = 12$ ($t' = 7.68$ ms), confirming that the monopoles with the polar-core vortex remain the excellent stability against decaying even though the quadrupole field is turned off. The results are interesting, which indicates that the SO coupling can protect such monopole structures during the time evolution in the absence of the external magnetic field.

APPENDIX G: DYNAMIC EVOLUTION OF THE SPIN TEXTURE

In Fig. 14 we investigate the dynamic evolution of the spin texture in order to more clearly ascertain the stabilities of the monopoles with the polar-core vortex. Figures 14(a1)–14(a3) indicate the dynamic of the spin texture in the presence of the quadrupole field. The spin texture remains the structure of the south magnetic pole during the time evolution, where the spin aligns with the radially inward hedgehog distribution in the x-y plane. Furthermore, when the quadrupole field is turned off, the spin texture of the south magnetic pole remains immobile; see Figs. 14(b1)–14(b3). Figure 14 further indicates that the monopoles with the polar-core vortex are stable during the time evolution. Finally, we further check the dynamics of the monopoles at different times such as a shorter time $t = 12$ ($t' = 7.6$ ms) and a longer time $t = 72$ ($t' = 46$ ms) (see Fig. 15), indicating that the monopoles have excellent
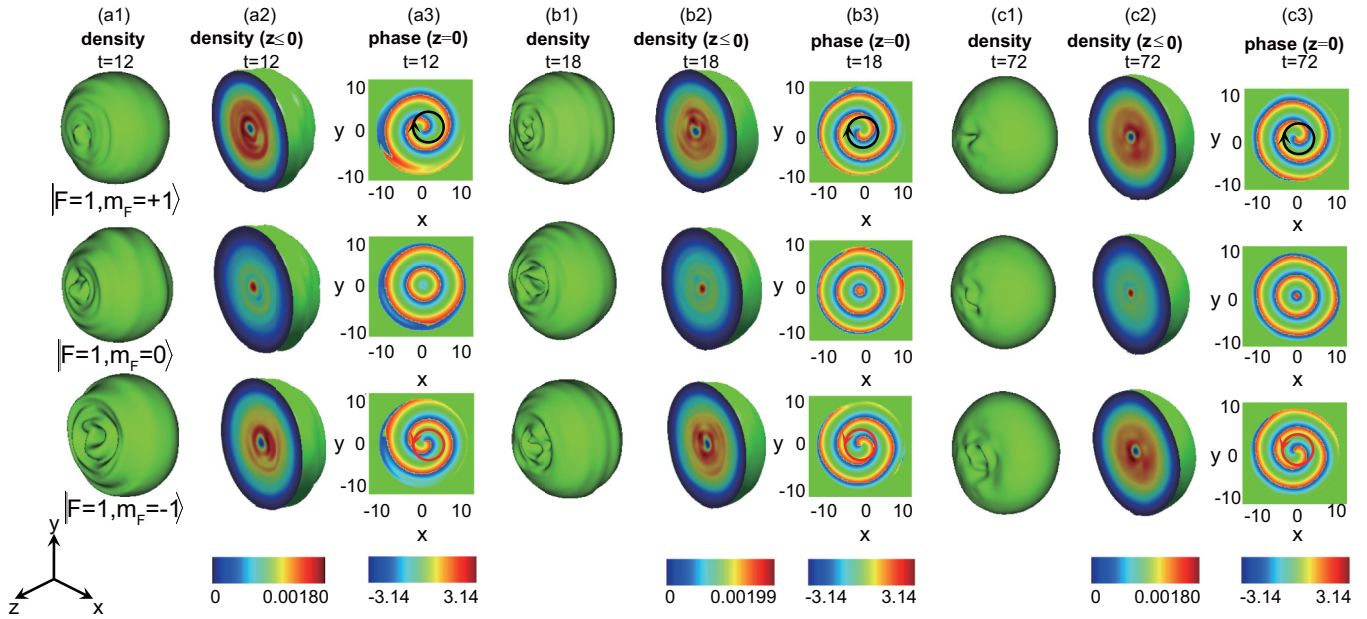
FIG. 15. Dynamics of the monopoles with the polar-core vortex at different times. (a1)–(a3) $t = 12$, (b1)–(b3) $t = 18$, and (c1)–(c3) $t = 72$. (a1), (b1), and (c1) Isosurface of particle densities. (a2), (b2), and (c2) Particle densities for $z \leqslant 0$. (a3), (b3), and (c3) Phase distributions in the $z = 0$ planes. The single vortex and antivortex are highlighted by the black and red circles, respectively. The simulation parameters are the same as the ones in Fig. 1 and the real time $t' = 0.64t$ ms.

stability even for a longer time. Figure 15 confirms that the monopoles with the polar-core vortex have very long lifetimes that are even beyond the time window of our simulations,

which allows for the facile experimental observation. We can expect that the monopoles with the polar-core vortex are able to exist in an atomic gas as a long-lived configuration.

[1] P. A. M. Dirac, Proc. R. Soc. London A **133**, 60 (1931).
[2] C. Castelnovo, R. Moessner, and S. L. Sondhi, Nature (London) **451**, 42 (2008).
[3] D. J. P. Morris *et al.*, Science **326**, 411 (2009).
[4] S. D. Pollard, V. Volkov, and Y. Zhu, Phys. Rev. B **85**, 180402(R) (2012).
[5] H. D. Zhou *et al.*, Nat. Commun. **2**, 478 (2011).
[6] D. l. Khomskii, Nat. Commun. **3**, 904 (2012).
[7] L. Bovo *et al.*, Nat. Commun. **4**, 1535 (2013).
[8] M. Cardoso, P. Bicudo, and P. D. Sacramento, Ann. Phys. **323**, 337 (2008).
[9] M. W. Ray *et al.*, Nature (London) **505**, 657 (2014).
[10] M. W. Ray *et al.*, Science **348**, 544 (2015).
[11] P. Goddard and D. I. Olive, Rep. Prog. Phys. **41**, 1357 (1978).
[12] L. Brekke, W. Fischler, and T. D. Imbo, Phys. Rev. Lett. **67**, 3643 (1991).
[13] B. L. G. Bakker, M. N. Chernodub, and M. I. Polikarpov, Phys. Rev. Lett. **80**, 30 (1998).
[14] J.-P. Martikainen, A. Collin, and K.-A. Suominen, Phys. Rev. Lett. **88**, 090404 (2002).
[15] V. Pietilä and M. Möttönen, Phys. Rev. Lett. **103**, 030401 (2009).
[16] J. E. Williams and M. J. Holland, Nature (London) **401**, 568 (1999).
[17] D. S. Hall *et al.*, Nat. Phys. **12**, 478 (2016).
[18] U. A. Khawaja and H. Stoof, Nature (London) **411**, 918 (2001).
[19] J.-y. Choi, W. J. Kwon, and Y.-i. Shin, Phys. Rev. Lett. **108**, 035301 (2012).

[20] Th. Busch and J. R. Anglin, Phys. Rev. A **60**, R2669 (1999).
[21] J. J. García-Ripoll, J. I. Cirac, J. Anglin, V. M. Pérez-García, and P. Zoller, Phys. Rev. A **61**, 053609 (2000).
[22] H. T. C. Stoof, E. Vliegen, U. Al Khawaja, Phys. Rev. Lett. **87**, 120407 (2001).
[23] C. M. Savage and J. Ruostekoski, Phys. Rev. A **68**, 043604 (2003).
[24] E. Ruokokoski, V. Pietilä, and M. Möttönen, Phys. Rev. A **84**, 063627 (2011).
[25] V. Pietilä and M. Möttönen, Phys. Rev. Lett. **102**, 080403 (2009).
[26] G. J. Conduit, Phys. Rev. A **86**, 021605(R) (2012).
[27] Y. M. Cho, Phys. Rev. Lett. **87**, 252001 (2001).
[28] D. D. Solnyshkov, H. Flayac, and G. Malpuech, Phys. Rev. B **85**, 073105 (2012).
[29] M. Kiffner, W. H. Li, and D. Jaksch, Phys. Rev. Lett. **110**, 170402 (2013).
[30] Y. J. Lin, K. Jiménez-García, and I. B. Spielman, Nature (London) **471**, 83 (2011).
[31] J. Ruseckas, G. Juzeliūnas, P. Öhberg, and M. Fleischhauer, Phys. Rev. Lett. **95**, 010404 (2005).
[32] X.-J. Liu, M. F. Borunda, X. Liu, and J. Sinova, Phys. Rev. Lett. **102**, 046402 (2009).
[33] J.-Y. Zhang, S.-C. Ji, Z. Chen, L. Zhang, Z.-D. Du, B. Yan, G.-S. Pan, B. Zhao, Y.-J. Deng, H. Zhai, S. Chen, and J.-W. Pan, Phys. Rev. Lett. **109**, 115301 (2012).
[34] S. C. Ji *et al.*, Nat. Phys. **10**, 314 (2014).

[35] D. L. Campbell, G. Juzeliūnas, and I. B. Spielman, Phys. Rev. A **84**, 025602 (2011).

[36] Z. H. Lan and P. Öhberg, Phys. Rev. A **89**, 023630 (2014).

[37] B. M. Anderson *et al.*, Phys. Rev. Lett. **108**, 235301 (2012).

[38] B. M. Anderson, I. B. Spielman, and G. Juzeliūnas, Phys. Rev. Lett. **111**, 125301 (2013).

[39] P. Wang, Z.-Q. Yu, Z. Fu, J. Miao, L. Huang, S. Chai, H. Zhai, and J. Zhang, Phys. Rev. Lett. **109**, 095301 (2012).

[40] L. W. Cheuk, A. T. Sommer, Z. Hadzibabic, T. Yefsah, W. S. Bakr, and M. W. Zwierlein, Phys. Rev. Lett. **109**, 095302 (2012).

[41] C. Wang, C. Gao, C.-M. Jian, and H. Zhai, Phys. Rev. Lett. **105**, 160403 (2010).

[42] S.-W. Su, I.-K. Liu, Y.-C. Tsai, W.-M. Liu, and S.-C. Gou, Phys. Rev. A **86**, 023601 (2012).

[43] C. F. Liu and W. M. Liu, Phys. Rev. A **86**, 033602 (2012).

[44] X. Q. Xu and J. H. Han, Phys. Rev. Lett. **107**, 200401 (2011).

[45] S. Sinha, R. Nath, and L. Santos, Phys. Rev. Lett. **107**, 270401 (2011).

[46] H. Hu, B. Ramachandhran, H. Pu, and X. J. Liu, Phys. Rev. Lett. **108**, 010402 (2012).

[47] S. Gopalakrishnan, I. Martin, and E. A. Demler, Phys. Rev. Lett. **111**, 185304 (2013).

[48] Y. Li, G. I. Martone, L. P. Pitaevskii, and S. Stringari, Phys. Rev. Lett. **110**, 235302 (2013).

[49] W. Han, G. Juzeliūnas, W. Zhang, and W.-M. Liu, Phys. Rev. A **91**, 013607 (2015).

[50] H. Pu, C. K. Law, S. Raghavan, J. H. Eberly, and N. P. Bigelow, Phys. Rev. A **60**, 1463 (1999).

[51] J. Stenger *et al.*, Nature (London) **396**, 345 (1998).

[52] E. G. M. van Kempen, S. J. J. M. F. Kokkelmans, D. J. Heinzen, and B. J. Verhaar, Phys. Rev. Lett. **88**, 093201 (2002).

[53] D. M. Stamper-Kurn and M. Ueda, Rev. Mod. Phys. **85**, 1191 (2013).

[54] F. Dalfovo and S. Stringari, Phys. Rev. A **53**, 2477 (1996).

[55] X.-F. Zhang, R.-F. Dong, T. Liu, W. M. Liu, and S.-G. Zhang, Phys. Rev. A **86**, 063628 (2012).

[56] W. Z. Bao and Q. Du, SIAM J. Sci. Comput. **25**, 1674 (2004).

[57] T. Mizushima, K. Machida, and T. Kita, Phys. Rev. Lett. **89**, 030401 (2002).

[58] T. Mizushima, N. Kobayashi, and K. Machida, Phys. Rev. A **70**, 043613 (2004).

[59] K. Kasamatsu, M. Tsubota, and M. Ueda, Phys. Rev. Lett. **93**, 250406 (2004).

[60] T. Kawakami, T. Mizushima, M. Nitta, and K. Machida, Phys. Rev. Lett. **109**, 015301 (2012).

[61] K. Kasamatsu, M. Tsubota, and M. Ueda, Phys. Rev. A **71**, 043611 (2005).

[62] T. Kita, Phys. Rev. Lett. **86**, 834 (2001).

[63] J. P. A. Devreese, J. Tempere Carlos, and A. R. Sá de Melo, Phys. Rev. Lett. **113**, 165304 (2014).

[64] L. F. Chibotaru *et al.*, Nature (London) **408**, 833 (2000).

[65] Y. Shin, M. Saba, M. Vengalattore, T. A. Pasquini, C. Sanner, A. E. Leanhardt, M. Prentiss, D. E. Pritchard, and W. Ketterle, Phys. Rev. Lett. **93**, 160406 (2004).

[66] J. A. M. Huhtamäki, M. Möttönen, T. Isoshima, V. Pietilä, and S. M. M. Virtanen, Phys. Rev. Lett. **97**, 110406 (2006).